

# Dynamics of line-driven disk winds in Active Galactic Nuclei.

Daniel Proga

LHEA, GSFC, NASA, Code 662, Greenbelt, MD 20771; proga@sobolev.gsfc.nasa.gov

James M. Stone

Department of Astronomy, University of Maryland, College Park, MD 20742; jstone@astro.umd.edu

Timothy R. Kallman

LHEA, GSFC, NASA, Code 662, Greenbelt, MD 20771; tim@xstar.gsfc.nasa.gov

## ABSTRACT

We present the results of axisymmetric time-dependent hydrodynamic calculations of line-driven winds from accretion disks in active galactic nuclei (AGN). We assume the disk is flat, Keplerian, geometrically thin, and optically thick, radiating according to the  $\alpha$ -disk prescription. The central engine of the AGN is a source of both ionizing X-rays and wind-driving ultraviolet (UV) photons. To calculate the radiation force, we take into account radiation from the disk and the central engine. The gas temperature and ionization state in the wind are calculated self-consistently from the photoionization and heating rate of the central engine.

We find that a disk accreting onto a  $10^8 M_\odot$  black hole at the rate of  $1.8 M_\odot \text{ yr}^{-1}$  can launch a wind at  $\sim 10^{16} \text{ cm}$  from the central engine. The X-rays from the central object are significantly attenuated by the disk atmosphere so they cannot prevent the local disk radiation from pushing matter away from the disk. However in the supersonic portion of the flow high above the disk, the X-rays can overionize the gas and decrease the wind terminal velocity. For a reasonable X-ray opacity, e.g.,  $\kappa_X = 40 \text{ g}^{-1} \text{ cm}^2$ , the disk wind can be accelerated by the central UV radiation to velocities of up to  $15000 \text{ km s}^{-1}$  at a distance of  $\sim 10^{17} \text{ cm}$  from the central engine. The covering factor of the disk wind is  $\sim 0.2$ . The wind is unsteady and consists of an opaque, slow vertical flow near the disk that is bounded on the polar side by a high-velocity stream. A typical column density through the fast stream is a few  $10^{23} \text{ cm}^{-2}$  so the stream is optically thin to the UV radiation. This low column density is precisely why gas can be accelerated to high velocities. The fast stream contributes nearly 100% to the total wind mass loss rate of  $0.5 M_\odot \text{ yr}^{-1}$ .

*Subject headings:* accretion disks – hydrodynamics – instabilities – outflows – galaxies: active – methods: numerical

## 1. Introduction

Many observed spectral features of active galactic nuclei (AGN) indicate that outflows are common in these systems. The prominent broad emission lines (BEL) in ultraviolet (UV) from H I, O VI, N V, C IV, and Si IV are the defining feature of quasars (Blandford, Netzer & Woltjer 1990; Osterbrock 1989), and they may be associated with a high velocity outflow. Fast outflows can also explain narrow UV absorption lines from highly ionized species – such as C IV and N V – observed in approximately half of the HST-observed Seyfert 1 galaxies (e.g., Crenshaw 1997). These narrow absorption lines are all blueshifted relative to the systemic velocity by 0 to  $-1600 \text{ km s}^{-1}$ . Recent ASCA observations show that in a small sample observed by HST and ASCA, all of the Seyfert galaxies with warm absorbers also show intrinsic UV absorption. A high-resolution X-ray observation of the Seyfert galaxy NGC 5548 obtained by Chandra shows strong, narrow absorption lines from highly ionized species (Kaastra et al. 2000). The lines are blueshifted by a few hundred  $\text{km s}^{-1}$  and they are reminiscent of the narrow absorption lines observed in the UV. Some QSOs also have intrinsic UV narrow-line absorbers with line-of-sight velocities as large as  $51000 \text{ km s}^{-1}$  (Hamann et al. 1997). Perhaps the most compelling evidence for fast outflows in QSOs are strong broad absorption lines (BALs) in the UV resonance lines of highly ionized species such as N V, C IV, and Si IV. The BALs are always blueshifted relative to the emission-line rest frame, indicating the presence of outflows from the active nucleus, with velocities as large as  $60000 \text{ km s}^{-1}$ .

A key constraint on any model for the origin of AGN outflows is the ionization balance. On one hand we observe very high luminosities in X-rays and the UV and on the other hand we observe spectral lines from moderately and highly ionized species. One wonders then how the gas avoids full photoionization and we see any spectral lines at all. Generally, two mechanisms have been proposed to resolve the so-called overionization problem: (i) the AGN outflows have filling factors less than one and consist of dense clouds and (ii) the filling factors equal one but the outflows are shielded from the powerful radiation by some material located between the central engine and the outflow (e.g., Krolik 1999, and below).

Many theoretical models have been proposed to explain outflows in AGNs. Comprehensive reviews of recent theoretical work on outflows in AGNs can be found in Arav, Shlosman & Weymann (1997). Several forces have been suggested to accelerate outflows in AGN, for example, gas pressure (e.g., Weymann et al. 1982; Begelman, de Kool & Sikora 1991), magneto-centrifugal force due to an accretion disk (e.g., Blandford & Payne 1982; Emmering, Blandford & Shlosman 1992; Königl & Kartje 1994; Bottorff et al. 1997), radiation pressure due to dust (e.g., Voit, Weymann & Korista 1993; Scoville & Norman 1995), and radiation pressure due to lines (e.g., Drew & Boksenberg 1984; Shlosman, Vitello & Shaviv 1985; Arav, Li & Begelman 1994; de Kool & Begelman 1995, hereafter dKB; Murray et al. 1995, hereafter MCGV). Most of these models avoid overionization of the wind by assuming high density clouds.

One plausible scenario for the AGN outflows is that radiation pressure on spectral lines drives a wind from an accretion disk around a black hole. The presence of the BALs themselves strongly indicates that substantial momentum is transferred from a powerful radiation field to the gas. A crucial clue to the origin of AGN outflows comes from the discovery of line-locking in BAL QSO spectra (e.g., Foltz et al. 1987). Weymann et al. (1991) discovered that a composite spectrum of their BAL QSO sample shows a double trough in the C IV  $\lambda 1549$  BAL, separated in velocity space by the N V  $\lambda 1240$ -Ly $\alpha$  splitting  $\sim 5,900 \text{ km s}^{-1}$  (see also Korista et al. 1993). In fact Arav & Begelman (1994, see also Arav et al. 1995 and Arav 1996) showed that an absorption hump in the C IV  $\lambda$  BAL is “the ghost of Ly $\alpha$ ” due to modulation of the radiation force by the strong emission in Ly $\alpha$ .

Our understanding of how line-driving produces powerful high velocity winds is based on the studies of winds in hot stars that radiate mostly in the UV (e.g., Castor, Abbott, Klein 1975, hereafter CAK; Abbott 1982). The essential concept underpinning these models is that the momentum is extracted most efficiently

from the radiation field via line opacity. With the inclusion of lines, CAK showed that the effective radiation force can increase by several orders of magnitude above that due to electron-scattering alone. Thus even a star that radiates at around 0.1% of its Eddington limit,  $L_{Edd}$  can have a strong wind. Up to now, however, it has been difficult to apply line-driven stellar wind models to QSOs because of the fundamental difference in geometry: stellar winds are to a good approximation spherically symmetric, whereas the wind in BAL QSOs likely arises from a flattened disk and is therefore axially symmetric.

Line-radiation driven disk wind models for BAL QSOs have been proposed by several authors. For example, MCGV studied a wind arising from a small distance from the central engine ( $\sim 10^{16}$  cm). Their model relies on the local disk radiation to launch gas from the disk and on the central radiation to accelerate the gas in the radial direction to high velocities. A key ingredient to this model is that the central engine radiation is attenuated by ‘hitchhiking’ gas located between the central engine and wind. Rather than showing from first principles the origin of this hitchhiking gas, they simply give plausible arguments for its existence. MCGV adopted assumptions that require the flow to be time-independent and restrict the flow geometry to a quasi 1-D radial flow. Other models of radiation-driven outflows in AGNs propose that the radiation force accelerates the wind that has been launched and kept at a low ionization state by *different* mechanisms. For example, the dKB model supposes that the wind is seated at a large distance ( $\sim 10^{18}$  cm) from the central engine. Because the disk is cool at these radii, the gas is not lifted from the disk by radiation pressure but by some alternative mechanism. Once the gas is high enough above the disk, the radiation force due to the central engine accelerates the gas to high velocity. The gas is not over-ionized in this model due to a small filling factor caused by strong magnetic fields which confine the dense clouds.

Recently it has been possible to model line-driven disk winds using 2-dimensional axisymmetric numerical hydrodynamical simulations (e.g., Pereyra, Kallman & Blondin 1997; PSD I; Proga 1999; Proga, Stone & Drew 1999, hereafter PSD II). All these models have been calculated for white dwarf accretion disks. PSD I found that line-driven disk winds are produced only when the effective luminosity of the disk (i.e., the luminosity of the disk times the maximum value of the force multiplier,  $L_D M_{max}$ ) exceeds the Eddington limit,  $L_{Edd}$ . If the dominant contribution to the total radiation field comes from the disk, then the outflow is intrinsically unsteady and characterized by large amplitude velocity and density fluctuations. On the other hand, if the total luminosity of the system is dominated by the central object, then the outflow is steady. In either case, PSD I and PSD II found that the structure of the wind consists of a dense, slow outflow, that is bounded on the polar side by a high-velocity, lower density stream. The flow geometry is controlled largely by the geometry of the radiation field – a brighter disk/central object produces a more polar/equatorial wind. Global properties such as the total mass loss rate and terminal velocity depend more on the system luminosity and are insensitive to geometry. The mass loss rate is a strong function of the effective Eddington luminosity and is of the same order of magnitude as that of a simple spherically-symmetric stellar wind (see also Proga 1999). Matter is fed into the fast stream from within a few central object radii. The terminal velocity of the stream is similar to that of the terminal velocity of a corresponding spherical stellar wind, i.e.,  $v_\infty \sim$  a few  $v_{esc}$ , where  $v_{esc}$ , is the escape velocity from the photosphere.

In this paper, we use the methods developed by PSD to study disk winds in AGNs. However to study AGNs winds, we need to relax some of the assumptions adopted by PSD. In particular, we can no longer assume the outflowing gas is isothermal, has a fixed ionization state, or is optically thin. Instead, we adopt a simplified treatment of photoionization, and radiative cooling and heating that allow us to compute self-consistently the ionization state, and therefore line force, in the wind.

Here we calculate a few disk wind models using our extensions to the PSD II method. We concentrate

on assessing how winds can be driven from a disk in the presence of very strong ionizing radiation. We describe our calculation in Section 2. We present our results in Section 3 and discuss them together with perceived limitations in Section 4. The paper ends, in section 5, with our conclusions.

## 2. Method

### 2.1. Hydrodynamics

To calculate the structure and evolution of a wind from a disk, we solve the equations of hydrodynamics

$$\frac{D\rho}{Dt} + \rho \nabla \cdot \mathbf{v} = 0, \quad (1)$$

$$\rho \frac{D\mathbf{v}}{Dt} = -\nabla P + \rho \mathbf{g} + \rho \mathbf{F}^{rad} \quad (2)$$

$$\rho \frac{D}{Dt} \left( \frac{e}{\rho} \right) = -p \nabla \cdot \mathbf{v} + \rho \mathcal{L}, \quad (3)$$

where  $\rho$  is the mass density,  $P$  is the gas pressure,  $\mathbf{v}$  is the velocity,  $e$  is the internal energy density,  $\mathcal{L}$  is the net cooling rate,  $\mathbf{g}$  is the gravitational acceleration of the central object,  $\mathbf{F}^{rad}$  is the total radiation force per unit mass. We adopt an adiabatic equation of state  $P = (\gamma - 1)e$ , and consider models with  $\gamma = 5/3$ .

Our calculations are performed in spherical polar coordinates  $(r, \theta, \phi)$ . We assume axial symmetry about the rotational axis of the accretion disk ( $\theta = 0^\circ$ ). However the  $\theta = 90^\circ$  axis is not coincident with the disk midplane. We allow this axis to be above the midplane, at the height,  $z_o$ , corresponding to the disk pressure scale height. Figure 1 shows a schematic representation of our computation domain. The offset enters our calculations in the computation of the gravity; for example the gravity has non-zero  $\theta$  component at  $\theta = 90^\circ$ , and in the computation of the Keplerian velocity along the  $\theta = 90^\circ$  axis.

This offset is introduced so that the bottom of our computational grid is located at the disk photosphere, where the wind is launched. Unlike the thin disk studied by PSD, the radiation dominated disk in AGN may have significant geometrical width. If the base of the computational grid is placed at the equatorial plane (midplane), this would require modeling the full internal structure of the disk, which is complex and turbulent (e.g., Balbus & Hawley 1998). Instead, we locate the base of the grid where the vertical radiation force due to electron scattering cancels out the vertical component of gravity.

A realistic description of the radiation field from the central engine would require detailed knowledge of the geometry of the flow near the central engine, which is beyond the scope of this investigation. Instead we model the central engine as a point source of radiation located at the origin of our computational grid (that is located a height  $z_o$  above the disk midplane). This implies the central engine has finite width, perhaps associated with a hot corona. We expect the high column density of the disk to attenuate radiation close to the  $\theta = 90^\circ$  plane.

Our standard computational domain is defined to occupy the radial range  $r_i = 100 r_* \leq r \leq r_o = 1000 r_*$ , where  $r_*$  is the inner radius of the disk, and the angular range  $0^\circ \leq \theta \leq 90^\circ$ . For comparison, we also calculate some models with the radial range  $50 r_* \leq r \leq 1000 r_*$  and with the radial range  $200 r_* \leq r \leq 1000 r_*$ . The  $r - \theta$  domain is discretized into zones. Our numerical resolution consists of 100

zones in each of the  $r$  and  $\theta$  directions, with fixed zone size ratios,  $dr_{k+1}/dr_k = 1.05$  and  $d\theta_l/d\theta_{l+1} = 1.087$ . Gridding in this manner ensures good spatial resolution close to the radiating surface of the disk and the inner boundary at  $r_i$ .

The boundary conditions are specified as follows. At  $\theta = 0$ , we apply an axis-of-symmetry boundary condition. For the outer radial boundary, we apply an outflow boundary condition. For the inner radial boundary  $r = r_*$  and for  $\theta = 90^\circ$ , we apply reflecting boundary conditions for the density, velocity and internal energy. To represent steady conditions in the photosphere at the base of the wind, during the evolution of each model we apply the constraints that in the first zone above the  $\theta = 90^\circ$  plane the radial velocity  $v_r = 0$ , the rotational velocity  $v_\phi$  remains Keplerian, and the density is fixed at  $\rho = \rho_0$  at all times. The initial conditions are as in PSD I except for the initial temperature profile which is described in detail in Section 2.3.

To solve eqs. 1-3 we use an extended version of the ZEUS-2D code (e.g., Stone & Norman 1992). The equation for the internal energy, eq. 3, is solved using the operator splitting method and the backward Euler scheme.

## 2.2. The radiation field and force

The geometry and assumptions needed to compute the radiation field from the disk and central object are as in PSD II (see also PSD I). The disk is flat, Keplerian, geometrically-thin and optically-thick. The disk photosphere is coincident with the  $\theta = 90^\circ$  axis. We specify the radiation field of the disk by assuming that the temperature follows the radial profile of the optically thick accretion disk (Shakura & Sunyaev 1973), and therefore depends on the mass accretion rate in the disk,  $\dot{M}_a$ , the mass of the black hole,  $M_{BH}$  and the inner edge of the disk,  $r_* = 3r_S$ , where  $r_S = 2GM_{BH}/c^2$  is the Schwarzschild radius of a black hole. In particular, the disk luminosity,  $L_D = 2\eta GM_{BH}\dot{M}_a/r_S$ , where  $\eta$  is the rest mass conversion efficiency.

The geometry of the central engine in AGNs is not well known. For simplicity, we consider the central engine as the most inner part of the accretion disk plus an extended corona. We refer to the corona as the central object. The radius of the central object is comparable with the inner radius of the disk and we assume that they formally are equal.

We express the central object luminosity  $L_*$  in units of the disk luminosity  $L_* = xL_D$ . In contrast to PSD I and PSD II, we allow for the situation when only some fraction of the central object luminosity takes part in driving a wind. We identify this fraction as the luminosity in the UV band,  $f_{UV}L_*$ . We refer to the fraction of the luminosity that is responsible for ionizing the wind to a very high state as the luminosity in the X-ray band,  $f_XL_*$ . For simplicity, we assume here that this fraction of the luminosity does not contribute to line driving of the wind. We call the luminosity in the remaining bands, mainly optical and infrared, as  $f_{O,IR}L_*$ . We assume that  $f_{O,IR}L_*$  is the part of the luminosity that does not change the dynamics of the wind. We stress that the fraction  $f_i$  is a numerical factor that we introduce here to parameterize the luminosity in each of those three domains. We set  $f_{OPT,IR}$  to zero in the remaining part of the paper as the central object is very hot. We take into account the irradiation of the disk by the central object, assuming that the disk re-emits all absorbed energy locally and isotropically. However we note that the contribution from irradiation is negligible for  $x \sim 1$  and large radii (see eq. 6 below).

We approximate the radiative acceleration due to lines (line force, for short) using a modified CAK

method. The line force at a point defined by the position vector  $\mathbf{r}$  is

$$\mathbf{F}^{rad,l}(\mathbf{r}) = \oint_{\Omega} M(t) \left( \hat{n} \frac{\sigma_e I(\mathbf{r}, \hat{n}) d\Omega}{c} \right) \quad (4)$$

where  $I$  is the frequency-integrated continuum intensity in the direction defined by the unit vector  $\hat{n}$ , and  $\Omega$  is the solid angle subtended by the disk and central object at the point. The term in brackets is the electron-scattering radiation force,  $\sigma_e$  is the mass-scattering coefficient for free electrons, and  $M(t)$  is the force multiplier – the numerical factor which parameterizes by how much spectral lines increase the scattering coefficient. In the Sobolev approximation,  $M(t)$  is a function of the optical depth parameter

$$t = \frac{\sigma_e \rho v_{th}}{|dv_l/dl|}, \quad (5)$$

where  $v_{th}$  is the thermal velocity, and  $\frac{dv_l}{dl}$  is the velocity gradient along the line of sight,  $\hat{n}$ .

We evaluate the radiation force in four steps. First, we calculate the intensity, the velocity gradient in the  $\hat{n}$  direction and then the optical depth parameter  $t$ . Second, we calculate the parameters of the force multiplier using a current value of the photoionization parameter,  $\xi$  adopting results of Stevens & Kallman (1990). Then we calculate the radiation force exerted by radiation along  $\hat{n}$ . Third, we integrate the radiation force over the solid angle subtended by the radiant surface. Finally, we correct the radiation force in the radial direction for the optical depth effects.

Our numerical algorithm for evaluating the line force for given parameters of the force multiplier, the third step, is described in PSD II. For a rotating flow, there may be an azimuthal component to the line force even in axisymmetry. However we set this component of the line force to zero because it is always less than other components (e.g., PSD II). See PSD I and PSD II for further details. Below we describe our calculations of the force multiplier for various conditions in the wind and our treatment of the optical depth effects on the radiation force.

In the disk plane at  $r = r_D$ ,  $I(\mathbf{r}, \hat{n})$  is the local isotropic disk intensity:

$$I_D(r_D) = \frac{3GM_{BH}\dot{M}_a}{8\pi^2 r_*^3} \left\{ \frac{r_*^3}{r_D^3} \left( 1 - \left( \frac{r_*}{r_D} \right)^{1/2} \right) + \frac{x}{3\pi} \left( \arcsin \frac{r_*}{r_D} - \frac{r_*}{r_D} \left( 1 - \left( \frac{r_*}{r_D} \right)^2 \right)^{1/2} \right) \right\}. \quad (6)$$

We consider only the hot part of the disk, where the local disk temperature,  $T_D \gtrsim$  a few  $10^3$  K. We then assume that all disk photons can contribute to the line force. The second term in the curly brackets corresponds to the contribution from the irradiation of a disk by a central object. For large radii and  $x \sim 1$ , the contribution from the irradiation is negligible compared to the intrinsic disk intensity (the first term in the curly brackets).

For radiation from the central object, the intensity may be written as:

$$I_* = \frac{L_*}{4\pi^2 r_*^2}. \quad (7)$$

We account for the fact that the central radiation consists of the two distinct spectral components by using the parameter  $f_i$ , where  $i = \text{X}$  or  $\text{UV}$ . We assume that the optical depth effects in the  $\theta$  direction are negligible for the central radiation in the two bands. Note that the  $\theta$  component of the radiation force due

to the central object is negligible in our computational domain because the domain is far from the object ( $r_* \ll r_i$ ). In the radial direction however, the column density can be high and the optical depth effects can be significant. We estimate the optical depth,  $\tau_i$  between the central source and a point in a wind from:

$$\tau_i = \int_0^r \kappa_i \rho dr, \quad (8)$$

where  $\kappa_i$  is the absorption coefficient representative for the  $i$  band, and  $r$  is the distance from the central source. We can treat the central object as a point source because our calculations are for  $r_*/r \ll 1$ . Then we calculate the radial component of the central radiation force due to lines from

$$(F_*^{rad,l})_r(\mathbf{r}) = f_{UV} \exp(-\tau_{UV}) \oint_{\Omega_*} M(t) \left( n_r \frac{\sigma_e I_*(\mathbf{r}, \hat{n}) d\Omega}{c} \right), \quad (9)$$

where  $\Omega_*$  is the central object solid angle. We also take into account the optical depth effects on the radial component of the electron-scattering force:

$$(F_*^{rad,e})_r(\mathbf{r}) = \{f_{UV} \exp(-\tau_{UV}) + f_X \exp(-\tau_X)\} \oint_{\Omega_*} \left( n_r \frac{\sigma_e I_*(\mathbf{r}, \hat{n}) d\Omega}{c} \right). \quad (10)$$

The attenuation of the X-ray radiation is calculated using  $\kappa_X = 40 \text{ g}^{-1} \text{ cm}^2$  for  $\xi \leq 10^5$  and  $\kappa_X = 0.4 \text{ g}^{-1} \text{ cm}^2$  for  $\xi > 10^5$ , while the attenuation of the UV radiation is calculated using  $\kappa_{UV} = 0.4 \text{ g}^{-1} \text{ cm}^2$  for all  $\xi$ .

A disk wind may also be optically thick to the UV radiation emitted by the disk. In particular, the flux along the radial direction near the disk can be significantly reduced due to high column density. We approximate this effect by multiplying the radial component of the disk radiation force by the attenuation factor  $\exp(-\tau_{UV})$ .

To calculate the force multiplier, we adopt the CAK analytical expression modified by Owocki, Castor & Rybicki (1988, see also PSD I)

$$M(t) = kt^{-\alpha} \left[ \frac{(1 + \tau_{max})^{(1-\alpha)} - 1}{\tau_{max}^{(1-\alpha)}} \right] \quad (11)$$

where  $k$  is proportional to the total number of lines,  $\alpha$  is the ratio of optically-thick to optically-thin lines,  $\tau_{max} = t\eta_{max}$  and  $\eta_{max}$  is a parameter determining the maximum value,  $M_{max}$  achieved for the force multiplier. Equation 11 shows the following limiting behavior:

$$\lim_{\tau_{max} \rightarrow \infty} M(t) = kt^{-\alpha} \quad (12)$$

$$\lim_{\tau_{max} \rightarrow 0} M(t) = M_{max}, \quad (13)$$

where  $M_{max} = k(1 - \alpha)\eta_{max}^\alpha$ . The maximum value of the force multiplier is a function of physical parameters of the wind and radiation field. Several studies have showed that  $M_{max}$  is roughly a few thousand for gas ionized by a weak or moderate radiation field (e.g., CAK; Abbott 1982; Stevens & Kallman 1990; Gayley 1995). As the radiation field becomes stronger and the gas becomes more ionized the force multiplier decreases asymptotically to zero.

The line force, in particular the parameters of the force multiplier depend on the ionization of the wind and the spectral energy distribution (SED) of the radiation field. Self-consistent calculations of the line-force for given wind conditions and the radiation require detailed calculations of the wind photoionization structure (e.g., CAK; Abbott 1982; Puls et al. 2000). The total line force includes contributions from  $> 10^5$

lines from many species. Such calculations in connection with the 2-D, time-dependent hydrodynamic calculations are not feasible. We therefore start by adopting the analytical formulae for the force multiplier due to Stevens & Kallman (1991). They studied the effects of X-ray ionization on the the radiative force experienced by the stellar wind in a massive X-ray binary (MXRB). Wind conditions in MXRBs differ somewhat from those in QSOs. In particular, the X-ray radiation in MXRBs can be well represented by a 10 KeV bremsstrahlung spectrum while the spectrum in QSOs is better fitted by power laws with different spectral indices at different spectral bands (e.g., Zheng et al. 1997; Laor et al. 1997). Nevertheless we adopt the Stevens & Kallman results as a first order approximation because the Compton temperature and the ionization structure are similar (Kallman & McCray 1982).

Using the photoionization code XSTAR, Stevens & Kallman found that the line force due to the radiation from the primary can be parameterized in terms of the CAK force multiplier. Their results show that the line force decreases sharply with increasing photoionization parameter:

$$\xi = \frac{4\pi\mathcal{F}_X}{n}, \quad (14)$$

where  $\mathcal{F}_X$  is the local X-ray flux,  $n$  is the number density of the gas ( $= \rho/(m_p\mu)$  , where  $m_p$  is the proton mass, and  $\mu$  is the mean molecular weight). Stevens & Kallman also found some simple analytical fits to their results that allowed them to express  $k$  and  $\eta_{max}$  as functions of  $\xi$ :

$$k = 0.03 + 0.385 \exp(-1.4\xi^{0.6}), \quad (15)$$

and

$$\log_{10} \eta_{max} = \begin{cases} 6.9 \exp(0.16 \xi^{0.4}) & \text{for } \log_{10} \xi \leq 0.5 \\ 9.1 \exp(-7.96 \times 10^{-3} \xi) & \text{for } \log_{10} \xi > 0.5 \end{cases} \quad (16)$$

The parameter  $\alpha = 0.6$  and does not change with  $\xi$ .

These expressions for the parameters of the force multiplier predict that  $M_{max}$  increases gradually from  $\sim 2000$  to  $5000$  as  $\xi$  increases from  $0$  to  $\sim 3$  and then drops to  $\sim 0.1$  at  $\xi = 1000$ . The line force becomes negligible for  $\xi \gtrsim 100$  because then  $M_{max} \sim 1$ .

To calculate the photoionization parameter, we first need to know the local X-ray flux  $\mathcal{F}_X$  (see eq. 14). We estimate  $\mathcal{F}_X$  assuming that the source of all X-rays is a point-like central object with the luminosity in the X-ray band,  $L_X = f_X L_*$ . Making the above simplifications, we can express the local X-ray flux as

$$\mathcal{F}_X = \exp(-\tau_X) \frac{L_X}{4\pi r^2}. \quad (17)$$

### 2.3. Radiation heating and cooling

We calculate the gas temperature assuming that the gas is optically thin to its own cooling radiation and that the abundances are cosmic (Withbroe 1971). The net cooling rate depends on the density,  $\rho$ , the temperature,  $T$ , the ionization parameter  $\xi$ , and the characteristic temperature of the X-ray radiation  $T_X$ . It is then possible to fit analytical formulae to the heating and cooling rate obtained from detailed photoionization calculations for various  $T_X$ ,  $T$ , and  $\xi$ . For example, Blondin (1994) found that for a 10 keV

bremsstrahlung spectrum, his fits typical agree with a detailed calculation (Blondin et al. 1990) to within 25%. Using Blondin’s result we can express the net cooling rate  $\mathcal{L}$  in equation 3 by

$$\rho\mathcal{L} = n^2(G_{Compton} + G_X - L_{b,l}) \text{ erg cm}^3 \text{ s}^{-1}, \quad (18)$$

where  $G_{Compton}$  is the rate of Compton heating/cooling,

$$G_{Compton} = 8.9 \times 10^{-36} \xi (T_X - T) \text{ erg cm}^{-3} \text{ s}^{-1}, \quad (19)$$

$G_X$  is the net rate of X-ray photoionization heating–recombination cooling

$$G_X = 1.5 \times 10^{-21} \xi^{1/4} T^{-1/2} (1 - T/T_X) \text{ erg cm}^{-3} \text{ s}^{-1} \quad (20)$$

and  $L_{b,l}$  is the rate of bremsstrahlung and line cooling

$$L_{b,l} = 3.3 \times 10^{-27} T^{1/2} + [1.7 \times 10^{-18} \exp(-1.3 \times 10^5/T) \xi^{-1} T^{-1/2} + 10^{-24}] \delta \text{ erg cm}^{-3} \text{ s}^{-1}. \quad (21)$$

The parameter  $\delta$  is introduced to control line cooling,  $\delta = 1$  represents optically thin cooling and  $\delta < 1$  represents the case when lines become optically thick and cooling is reduced.

As we mentioned in Section 2.1, we use the same initial and boundary conditions as in PSD I. However we here also calculate the evolution of the internal energy. We specify the boundary conditions and the initial conditions for  $e$  as follows. For the temperature at the base of the wind, in the first grid zone above the  $\theta = 90^\circ$  plane, we adopt the solution for the steady state disk. Adopting the assumption that the local disk intensity is a black body and using eq. 6, the disk temperature is:

$$T_D(r_D) = (\pi I_D(r_D)/\sigma)^{1/4}. \quad (22)$$

Then we calculate the internal energy from

$$e_o(r_D) = \frac{\rho_o k T(r_D)}{\mu m_p (\gamma - 1)}, \quad (23)$$

where  $\rho_o$  is the density in the first grid zone above the  $\theta = 90^\circ$  plane. We consider models with  $\mu = 1$ . We initialize the internal energy at other locations by assuming that the gas temperature at a given radius is the same as at the disk temperature (i.e.,  $T(r, \theta) = T_D(r \sin \theta)$  for all  $\theta$ ) and using initial value of the density (see PSD I). Consistent with the boundary conditions for other gas quantities (see Sect. 2.1) we apply the constraint that in the first zone above the  $\theta = 90^\circ$  plane the internal energy  $e = e_o$  at all times. We find only the initial, transient evolution of the wind is affected by this choice of initial temperature conditions.

Our treatment of radiative heating and cooling is most likely valid in a low density and high photoionization parameter regime. For a high density and low photoionization parameter regime our treatment will likely underestimate the temperature because we oversimplify line cooling by not properly taking into account optical depth effects. In dense regions, our scheme therefore may yield a very low gas temperature (e.g.,  $T \ll 1000$  K). In such cases we set the lower limit for the temperature assuming that the gas is in local thermodynamical equilibrium, i.e., the gas temperature equals the local disk radiation temperature. Specifically, if at the  $(r, \theta)$  wind point the temperature from eq. 3 is less than  $T_D(r \sin \theta)$  then we replace it with  $T_D(r \sin \theta)$ .

### 3. Results

We specify our models by several parameters. In all our calculations we assume the mass of the non-rotating black hole,  $M_{BH} = 10^8 M_{\odot}$  and the rest mass conversion efficiency,  $\eta = 0.06$  typical for AGN. To determine the radiation field from the disk, we assume the mass accretion rate  $\dot{M}_a = 1.8 M_{\odot} \text{ yr}^{-1}$ . These system parameters yield the disk Eddington number,  $\Gamma_D = 0.5$ , the disk inner radius,  $r_* = 8.8 \times 10^{13} \text{ cm}$  and the orbital period at the inner edge of the disk,  $\tau = \sqrt{\frac{r_*^3}{GM_{BH}}} = 7.22 \times 10^3 \text{ sec}$ . We set the offset of the computational domain,  $z_o = H_D \approx 3\Gamma_D$  that corresponds to the half width of the radiation pressure dominated disk at large radii (e.g., Shakura & Sunyaev 1973). The radiation field from the central engine is specified by the additional parameters:  $x = 1$ ,  $f_{UV} = 0.5$ ,  $f_X = 0.5$ . As we discussed above the SED of the ionizing radiation is not well known, our choice of values for  $f_{UV}$  and  $f_X$  is guided by the results from Zheng et al. (1997) and Laor et al. (1997). To calculate the line force we adopt the force multiplier parameter  $\alpha = 0.6$ . We calculate the remaining parameters of the multiplier, i.e.,  $k$  and  $\eta_{max}$  as functions of the photoionization parameter,  $\xi$  using eqs 15 and 16. The force multiplier depends only formally on the thermal speed,  $v_{th}$  which we set to  $20 \text{ km s}^{-1}$ , i.e., the thermal speed of a hydrogen atom at the temperature of 25000 K (Stevens & Kallman 1990). To calculate the gas temperature, we assume the temperature of the X-ray radiation,  $T_X = 10 \text{ KeV}$  and the line cooling parameter  $\delta = 1$ .

We adopted a generalized CAK method to calculate a disk wind driven by the line force (PSD II). The CAK method has been developed for OB stars with photospheres dominated by gas pressure (the inner atmosphere is in hydrostatic equilibrium), and they radiate most of their energy in the UV band. We chose the radial extent of the computational domain (i.e.,  $100 r_* \leq r \leq 1000 r_*$ ) keeping in mind that the disk atmosphere should satisfy these two conditions, however some compromises had to be done. For example, the disk temperature at  $100 r_* = 8.8 \times 10^{15} \text{ cm}$  is 8200 K while at  $1000 r_* = 8.8 \times 10^{16} \text{ cm}$  is 1500 K using our disk parameters. We realize that according to the  $\alpha$ -disk model the disk emits mostly in the UV band down to the radius of  $\sim 10 r_*$  where its effective temperature is 50000 K. However the disk at this small radius is likely radiation dominated (e.g., Shakura & Sunyaev 1973; Svensson & Zdziarski 1994). On the other hand, the disk atmosphere at radius  $1000 r_*$  and the effective temperature of 1500 K, radiates most of its energy in the infrared band. Nevertheless we chose a large value for the outer edge of the computational domain to make sure that the domain includes most of the acceleration zone of the disk wind launched from the inner disk and the wind velocity at the outer edge well represents the wind terminal velocity.

Figure 2 shows the instantaneous density, temperature and photoionization parameter distributions and the poloidal velocity field of the model. After 12.6 years ( $\sim 5.5 \times 10^4 \tau$ ), the disk material fills the grid for  $\theta \gtrsim 70^\circ$  and remains in that region for the rest of the run, i.e., over next 47.7 years. Figure 2 shows results after 14.6 years. Although the flow is time-dependent the gross properties of the flow (e.g., the mass loss rate and the radial velocity at the outer boundary), settle down to steady time-averages over timescales on the order of 3 years. Our calculation follows (i) a hot, low density flow in the polar region (ii) a dense, warm and fast equatorial outflow from the disk, (iii) a transitional zone in which the disk outflow is hot and struggles to escape the system.

In the polar region, the density is very small and close to the lower limit that we set on the grid, i.e.,  $\rho_{min} = 10^{-20} \text{ g cm}^{-3}$ . The line force is negligible because the matter is highly ionized as indicated by a very large photoionization parameter ( $\sim 10^7$ ). The gas temperature is close to the temperature of the X-ray radiation, again indicative of highly ionized gas. The matter in the polar region is pulled by the gravity from the outer boundary and it is an artifact of the boundary conditions. Overall this region of the very low density is not relevant to our analysis as it has no effect on the much denser disk flow.

The equatorial region is distinctly different. In the inner part of the disk (i.e., for  $r \sim r_i$ ), the density at the wind base is high,  $\sim 10^{-13} \text{ g cm}^{-3}$ . Thus the photoionization parameter is low despite the strong

central radiation. However as the flow from the inner part of the disk is accelerated by the line force its density decreases and the gas temperature and the photoionization parameter increase. Subsequently the gas becomes fully ionized and loses all of driving lines before it reaches the escape velocity and therefore falls on the central object/inner disk. Although this gas does not produce a wind, its primary effect is to shield the gas at larger radii. Thus the wind consists of gas accelerated by the line force at larger radii, in fact driving of the disk wind extends over all radii at which the intrinsic disk radiation is large enough to launch gas.

The poloidal velocity (Fig. 2c) shows that the gas streamlines are perpendicular to the disk over some height that increases with radius. The streamlines then bend away from the central object and converge. The region where the flow is moving almost radially outward is associated with a high-velocity, high density stream. This fast stream contributes  $\sim 100\%$  to the total mass loss rate,  $\dot{M}_W = 0.5 \text{ M}_\odot \text{ yr}^{-1}$ . We note that the mass loss rate can increase by a factor of a few when a knot is crossing the outer boundary.

The fast stream is variable. In the upper envelope of the disk wind there is large velocity shear between the higher density fast stream moving outward and the lower density fast gas moving inward. Our simulations show that this shear gives rise to Kelvin-Helmholtz instabilities. The instabilities generate knots that propagate along the fast stream at  $\sim 10000 \text{ km s}^{-1}$ . Figure 2a shows an example of such a knot at  $r \sim 750 r_*$  and  $z \sim 200 r_*$ , in the figure coordinates. The density contrast between the knot and the fast stream is  $\sim 2$  orders of magnitude. The knots generator is episodic and is inherent to the fast stream. We observed the generation of 19 knots over 60.4 years. In other words, a knot is produced every  $\sim 3$  years.

Figure 3 presents a sequence of density maps showing time evolution of the outflow from Figure 2 after 13.3, 14.6 and 16.47 years, left, middle and right panel respectively. Note that the middle panel from Figure 3 is the same as the top left panel from Figure 2. Figure 3 well illustrates variability in the outflow, in particular, generation of a knot in the fast stream at  $r \sim 450 r_*$  and  $z \sim 100 r_*$  (left panel), the well-formed knot at  $r \sim 750 r_*$  and  $z \sim 200 r_*$  (middle panel), and the time when the knot left the gird at  $r \sim 950 r_*$  and  $z \sim 300 r_*$ , and the fast stream is fairly smooth in between episodes with knots (right panel). The time dependence in the region close to the disk, bounded by the fast stream resembles outward propagation of a wave at the begin of evolution but becomes more complex with time as elements of the flow move both upwards and downwards.

Figure 4 presents the run of the density, radial velocity, photoionization parameter and column density as a function of the polar angle,  $\theta$  at the outer boundary,  $r_o = 8.8 \times 10^{16} \text{ cm}$  from Figure 2. The column density is given by:

$$N_H(\theta) = \int_{r_i}^{r_o} \frac{\rho(r, \theta)}{\mu m_p} dr. \quad (24)$$

The gas density is a very strong function of angle for  $\theta$  between  $90^\circ$  and  $65^\circ$ . The density drops by 8 orders of magnitude between  $\theta = 90^\circ$  and  $\theta \sim 89^\circ$ , as might be expected of a density profile determined by hydrostatic equilibrium. For  $70^\circ \lesssim \theta \lesssim 89^\circ$ , the wind domain,  $\rho$  varies between  $10^{-19}$  and  $10^{-17} \text{ g cm}^{-3}$ . For  $\theta \lesssim 70^\circ$ , density decreases gradually to so low a value that it becomes necessary to replace it by the numerical lower limit  $\rho_{min}$ . The radial velocity at  $1000 r_* = 8.8 \times 10^{16} \text{ cm}$  has a broad peak for  $72^\circ \lesssim \theta \lesssim 82^\circ$  with the maximum of  $15000 \text{ km s}^{-1}$  at  $\theta \sim 75$ . On both side of the peak the velocity is close to zero.

The photoionization parameter is very high,  $\sim 10^7$ , for  $\theta \lesssim 70^\circ$  because of the very low density. However it drops by 15 orders of magnitude between  $70^\circ \lesssim \theta \lesssim 75^\circ$  and stays at a very low level for  $\theta > 75^\circ$ . The column density changes less dramatically with angle. Between the pole and  $\theta \lesssim 67^\circ$ ,  $N_H$  is

less than  $10^{22} \text{ cm}^{-2}$ . For  $\theta > 67^\circ$ ,  $N_{\text{H}}$  increases gradually with  $\theta$ , it reaches value of  $10^{24} \text{ cm}^{-2}$  at  $\theta \sim 80^\circ$ . For  $80^\circ \lesssim \theta \lesssim 89^\circ$ ,  $N_{\text{H}}$  varies between  $10^{24} \text{ cm}^{-2}$  and  $10^{26} \text{ cm}^{-2}$ .

Our model shows that (i) the intrinsic disk radiation can launch a wind and (ii) the central object radiation can accelerate the disk wind to very high velocities. We have checked how these main results are sensitive to the model parameters. For a fixed disk atmosphere and central radiation source, the most important parameter of our model is the optical depth for the X-rays from the central object. Therefore we have run several tests with various X-ray opacities for  $\xi < 10^5$ :  $\kappa_X = 0.4 \text{ g}^{-1} \text{ cm}^2$  and  $\kappa_X = 4 \text{ g}^{-1} \text{ cm}^2$ . The former case is most conservative because it corresponds to the case when the X-ray optical depth is reduced to the Thomson optical depth. We found that in both test runs the X-ray radiation is significantly attenuated so the line force can launch a disk outflow. However the flow velocity never exceeds the escape velocity because the X-rays fully ionize the gas close to the disk and produces a hot corona with complex velocity field but which does not escape the system. We conclude then that the disk atmosphere can 'shield' itself at least to the extent that the local disk radiation can launch gas off the disk photosphere.

The two test runs also illustrate how robust is our second result: the central radiation accelerates the wind to very high velocities. For this to happen the column density,  $N_{\text{H}}$  must be large enough to reduce the X-ray radiation but too not large to reduce the UV flux in the radial direction. In other words, this requires  $\tau_X > 1$  and at the same time,  $\tau_{UV} \ll 1$ .

The test run with  $\kappa_X = 0.4 \text{ g}^{-1} \text{ cm}^2$  corresponds to the situation where  $\tau_X = \tau_{UV}$ . Thus the disk gas that is sufficiently shielded from the X-rays is also shielded from the UV photons from the central object. Such gas can only be lifted from the disk surface by the disk UV radiation but fails to gain momentum in the radial direction.

The fact that the disk wind can be launched without *external* shielding material implies that our solution can depend on the location of the inner computational radius,  $r_i$ . We have run several tests with  $r_i = 50r_*$  and  $r_i = 200r_*$  to check this (the remaining model parameters were as in the models shown in Figure 1 and 2). We found that the location of the inner edge,  $r_i$  affects the properties of the wind but not the fact the wind is produced. For example, the wind opening angle,  $\omega$ , is  $25^\circ$ ,  $15^\circ$  and  $8^\circ$  for  $r_i = 50, r_*, 100r_*$  and  $200r_*$ , respectively. The maximum radial velocity at the outer boundary decreases from  $20000 \text{ km s}^{-1}$  through,  $15000 \text{ km s}^{-1}$  to  $5000 \text{ km s}^{-1}$  for above sequence of decreasing  $r_i$ . The mass loss rate also decreases with  $r_i$  from  $0.6 \text{ M}_\odot \text{ yr}^{-1}$  through  $0.5 \text{ M}_\odot \text{ yr}^{-1}$  to  $0.2 \text{ M}_\odot \text{ yr}^{-1}$ .

#### 4. Discussion

Our calculations show that the UV emitting accretion disk can launch a wind that will shield itself from the strong ionizing radiation emitted from the central object. The self-shielding is quite robust because the external radiation does not penetrate the disk down to the region where the line force becomes important and pushes matter away from the photosphere. We illustrated the robustness of the self-shielding by changing relevant model parameters. We also note that a similar effect was observed by Stevens & Kallman (1990) and Stevens (1991). They studied the effects of X-ray ionization on the radiative force experienced by the stellar wind in a MXRB. They calculated the detailed photoionization structure of the line-driven wind for various X-ray luminosities without optical depth effects (Stevens & Kallman 1990) and with optical depth effects (Stevens 1991). Additionally, they considered irradiation at various directions including the normal to the mass losing photosphere. In none of the models the irradiation penetrated below the so-called

wind critical point where, in the CAK type models, the wind mass loss rate is determined. They found, as we did, that the irradiation can severely decrease the wind velocity in the supersonic portion of the flow.

We model here a line-driven wind from a disk that is flat, Keplerian, geometrically-thin and optically-thick. For the temperature at the base of the wind, in the first grid zone above the  $\theta = 90^\circ$  plane, we adopt the solution for the steady state  $\alpha$  disk. We calculate the local disk intensity as if it emits as a black body. In all our calculations, we treat the regions for  $\theta \sim 90^\circ$  as if they are gas pressure dominated. We find that our results depend on the inner radius of the computational domain. This dependence is likely an artifact of one or more of our assumptions. For example, for very high luminosities the inner part of the disk is dominated by the radiation pressure. For the parameters adopted here, namely  $\Gamma = 0.5$ , the inner radius of a gas pressure dominated disk is  $\sim 10^{16}$  cm (e.g., Svensson & Zdziarski 1994). The structure of the radiation dominated disks is not well known. We expect, however, that incorporating the radiation dominated part of the disk into our calculation will change the condition of the base of the wind, for example, the gas density and the UV flux might be reduced. These changes might affect the solution for the wind, in particular, the wind mass flux. We plan to explore these issues in a future paper.

To calculate the disk surface temperature and intensity, we took into account the irradiation of the disk by the central object. However the contribution from the irradiation is negligible compared to the disk intrinsic temperature because we considered a flat disk at large radii. Additionally, the high column density of the disk wind, that we found in our models, implies that the irradiating flux will be significantly attenuated by the wind before it reaches the disk surface. We anticipate that the last effect will significantly reduce disk irradiation regardless of the shape of the disk surface – flat or flaring. Detailed NLTE photoionization calculations are required to determine what fraction of the central radiation will reach the surface of a mass losing disk. A complete treatment of disk irradiation is difficult also because it is not obvious a priori whether the radiation incident on the disk is completely thermalized and re-radiated isotropically or it is scattered off the disk atmosphere or both.

Our calculations show that a line-driven disk wind model offers a promise of explaining outflows in AGNs. However they also illustrate some problems with this model. For example, as dKB pointed out in discussing MCGV's model, a very small radius at which the disk wind is launched also implies a very small size to BELR because BELR lies inside or is cospatial with BALR. The small scales in turn imply short crossing time of the BALR, of order of a month or so, and it is difficult to understand that the highly complex kinematical structures that BALs often exhibit do not appear to vary on timescales of 10 years (Barlow 1994).

Our axisymmetric 2D models show that the disk wind is unsteady and generates dense knots every 3 years. These knots will correspond to rings in 3D. However in fully 3D calculations the rings may break down to spirals or clouds or both. The breaking down of the rings will change the density contrast between them and the rest of the wind. Thus it is not clear if we would be able to see any spectral signature of density fluctuations in the wind. Detail calculations of line profiles are required to check this point. Additionally, detailed photoionization calculations are required to check if the full range of ions observed to show BAL profiles can be explained: BALs from ions with ionization potentials as low as of O III or lower and as high as of O VI.

To produce a fast wind the ratio between  $\tau_X$  to  $\tau_{UV}$  is very important. The low ratio gives a slow disk wind whereas the high ratio gives a fast wind. This result is consistent with the observed anti-correlation for QSOs between the relative strength of the soft X-ray flux and the CIV absorption equivalent width (e.g., Brandt, Laor & Wills 2000). However there is an upper limit for the X-ray attenuation, or the column

density between the X-ray source and wind, namely for  $N_H \gtrsim 10^{24} \text{ cm}^{-2}$  ( $\tau_X \gg 1$ ) the gas is well shielded from the X-rays but at the same time it is also shielded from any other radiation from the central engine including the UV radiation. In this case, the line force from the central engine could be so much reduced that it may not accelerate the gas to high radial velocities and no strong wind will be produced.

Some of the emission-line properties of QSOs could be explained as a correlation between luminosity and the slope of the ionizing spectrum, i.e., lower luminosity objects have harder spectra (e.g., Boroson & Green 1992). Using our parameterization of the AGN radiation, this QSO's property can be represented by increasing  $f_X$  in expense of  $f_{UV}$  when we reduce the luminosity. Such a choice of model parameters will increase the strength of X-ray ionizing radiation in comparison to the UV driving radiation. Consequently a disk wind should be weaker and slower as some of our test runs indicate.

Boroson & Green (1992) argue that the dominant source of variation in the observed properties of low redshift QSOs is not driven by external orientation but rather by the fraction of the Eddington luminosity at which the object is emitting (our parameter  $\Gamma_D$ ). We plan to examine the parameter space of our models to define the major trends in disk wind behavior that will help us to explain the observational trends found in various AGNs.

## 5. Conclusions

We have studied radiation driven winds from luminous accretion disks using numerical methods to solve the two-dimensional, time-dependent equations of hydrodynamics. In so doing we have accounted for the radiation force due to spectral lines using a generalized multidimensional formulation of the Sobolev approximation. Additionally we have taken into account the effects of the strong central radiation on the wind photoionization structure and thermodynamics.

We find that the local disk radiation can launch a wind from the disk despite strong ionizing radiation from the central object. The central radiation may overionize the supersonic portion of the flow and severely reduce the wind velocity. To produce a fast disk wind the wind X-ray opacity must be higher than the UV opacity by  $\gtrsim 2$  orders of magnitude.

Our calculations of a wind from a disk accreting onto a  $10^8 M_\odot$  black hole at the rate of  $1.8 M_\odot \text{ yr}^{-1}$  show that the radiation force from an accretion disk can launch a self-shielding wind from a radius of  $\lesssim 10^{16} \text{ cm}$  while the strong UV radiation from the central object can radially accelerate the disk wind to velocities  $\sim 15000 \text{ km s}^{-1}$ , for the X-ray opacity of  $40 \text{ g}^{-1} \text{ cm}^2$ . The disk wind domain is intrinsically unsteady and its covering factor is  $\sim 0.2$ . The wind mass loss is  $0.5 M_\odot \text{ yr}^{-1}$  which is a significant fraction of the mass accretion rate. The strong X-ray radiation from a central object completely ionizes the polar region and only a thin layer above the upper envelope of the disk wind. The disk wind immediately below the upper envelope can be characterized as a fast, high-density stream which is reminiscent of the PSD disk wind solution dominated by the driving radiation from a bright central object. The column density of the fast stream is between  $10^{22} \text{ cm}^{-2}$  and  $10^{24} \text{ cm}^{-2}$  so the stream is optically thin to the UV radiation and this is precisely why it can be accelerated to high velocities. On the other hand, the part of the wind bounded by the fast stream, closer to the disk, is slow and is reminiscent of the PSD solution dominated by the driving radiation from the disk. The column density of the slow wind is  $> 10^{24} \text{ cm}^{-2}$  so it is completely shielded from the central radiation, both the X-rays and the UV photons.

ACKNOWLEDGEMENTS: We would like to thank J.E. Drew for useful discussions. The work presented in this paper was initiated while DP was a PPARC Research Associate at Imperial College, London and it was performed while DP held a National Research Council Research Associateship at NASA/GSFC. Computations were supported by NASA grant NRA-97-12-055-154.

## REFERENCES

Abbott, D.C. 1982, ApJ, 259, 282

Arav, N. 1996, ApJ, 465, 617

Arav, N., Korista, T.K., Barlow, T. A., & Begelman, M. C. 1995, Nature, 376, 576

Arav N., & Begelman, M.C. 1994, ApJ, 434, 479

Arav N., Li, Z.Y., & Begelman M.C. 1994, ApJ, 432, 62

Arav N., Shlosman I., & Weymann. R. ed. 1997, in ASP Conf. Ser. 128, Mass Ejection from Active Galactic Nuclei, (San Francisco: ASP)

Barlow, T.A. 1994, PASP, 106, 548

Balbus, S.A., & Hawley, J.F. 1998, Rev. Mod. Phys., 70, 1

Begelman, M.C., de Kool, M., & Sikora, M. 1991, ApJ, 382, 416

Blandford, R.D., Netzer H., Woltjer L., Courvoisier T., & Mayor M. 1990, Active Galactic Nuclei, (Berlin: Springer)

Blandford, R.D., Payne, D.G. 1982, MNRAS, 199, 883

Blondin, J.M. 1994, ApJ, 435, 756

Blondin, J.M., Kallman, T.R., Fryxell, B.A., & Taam, R.E. 1990, ApJ, 356, 591

Boroson, T.A., & Green, R.F. 1994, ApJS, 80, 109

Bottorff, M., Korista, K.T., Shlosman, I., & Blandford, D.R. 1997, ApJ, 479, 200

Brandt, W.N., Laor, A., & Wills, B. J. 2000, ApJ, 528, 637

Castor, J.I., Abbott, D.C., Klein, R.I. 1975, ApJ, 195, 157 (CAK)

Crenshaw, D.M. 1997, in ASP Conf. Ser. 128, Mass Ejection from Active Galactic Nuclei, ed. N. Arav, I. Shlosman, & R. Weymann (San Francisco: ASP), p. 121

de Kool, M., & Begelman, M.C. 1995, APJ, 455, 448 (dKB)

Drew, J.E., & Boksenberg, A. 1984, MNRAS, 211, 813

Emmering, R.T., Blandford, R.D., & Shlosman, I. 1992, ApJ, 385, 460

Foltz, C.B., Weymann, R.J., Morris, S.L., & Turnshek, D.A. 1987, ApJ, 317, 450

Gayley, K.G. 1995, ApJ, 454, 410

Hamann, F., Barlow, T.A., Cohen, R.D., Junkkarinen, V., & Burbidge, E.M. 1997, in ASP Conf. Ser. 128, Mass Ejection from Active Galactic Nuclei, ed. N. Arav, I. Shlosman, & R. Weymann (San Francisco: ASP), p. 19

Kaastra, J.S., Mewe, R., Liedahl, D.A., Komossa, S. & Brinkman, A.C. 2000, A&A, 354, L83

Kallman, T.R., & McCray, R. 1982, ApJS, 50 263

Königl, A., & Kartje, J. F. 1994, ApJ, 434, 446

Korista, K.T., Voit, G.M. Morris, S.L., & Weymann R.J. 1993, ApJS, 88, 357

Krolik, J.H. 1999, Active galactic nuclei: from the central black hole to the galactic environment, Princeton, N.J.: Princeton University Press

Laor, A., Fiore, F., Elvis, E., & Wilkes B.J., & McDowell J.C. 1997, ApJ, 477, 93

Murray, N., Chiang, J., Grossman, S.A., & Voit, G.M. 1995, ApJ, 451, 498 (MCVG)

Osterbrock, D.E. 1989, Astrophysics of Gaseous Nebulae and Active Galactic Nuclei (Mill Valley: University Science Books), chap. 11

Owocki, S.P., Castor J.I., & Rybicki, G.B. 1988, ApJ, 335, 914

Pereyra, N.A., Kallman, T.R., & Blondin, J.M. 1997, ApJ, 477, 368

Proga, D. 1999, MNRAS, 304, 938

Proga, D., Stone J.M., & Drew J.E. 1998, MNRAS, 295, 595 (PSD I)

Proga, D., Stone J.M., & Drew J.E. 1999, MNRAS, 310, 476 (PSD II)

Puls, J., Springmann, U., & Lennon, M. 2000, A&AS 141, 23

Scoville, N., & Norman, C. 1995, ApJ, 451, 510

Shakura N.I., & Sunyaev R.A. 1973 A&A, 24, 337

Shlosman, I., Vitello, P., & Shaviv, G. 1985, ApJ, 294, 96

Stevens, I.R. 1991, ApJ, 379, 310

Stevens, I.R., & Kallman T.R. 1990, ApJ, 365, 321

Stone, J.M., Norman, M.L. 1992, ApJS, 80, 753

Svensson, R., & Zdziarski, A.A. 1994, ApJ, 436, 599

Voit, G.M., Weymann, R.J., & Korista, K.T. 1993, ApJ, 413, 95

Weymann, R.J., Morris, S.L., Foltz, C.B., & Hewett, P.C. 1991, ApJ, 373, 23

Weymann, R.J., Scott, J.S., Schiano, A.V.R., & Christiansen, W.A. 1982, ApJ, 262, 497

Withbroe, G. 1971, in The Menzel Symposium on Solar Physics, Atomic Spectra, and Gaseous Nebulae, ed. K.B. Gebbie (NBS Spec. Pub. 353; Washington, D.C.: NBS), p. 127

Zheng, W., Kriss, G.A., Telfer, R.C., Grimes, J.P., & Davidsen, A.F. 1997, ApJ, 475, 469

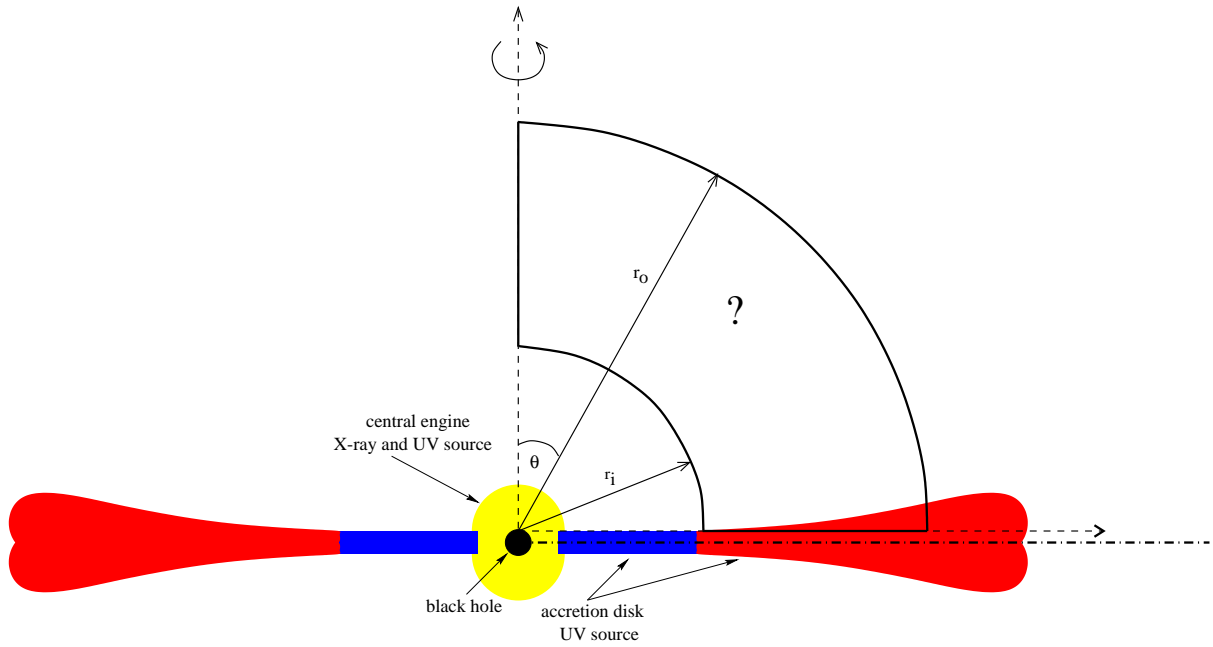


Fig. 1.— The framework of our two-dimensional hydrodynamical calculations for a line-driven disk wind. The drawing is not to scale. We assume the disk is flat, Keplerian, geometrically thin, and optically thick. The radiation pressure dominated disk is represented by the blue regions while the gas pressure dominated disk is represented by the red regions. The black hole is represented by the black circle while the X-ray source, is marked by the yellow region. The dashed line perpendicular to the disk is the disk rotational axis. Our computational domain is marked by solid lines. The  $\theta = 90^\circ$  axis, the dashed line perpendicular to the rotational axis, is located above the disk midplane, the dot-dashed line. The offset of the  $\theta = 90^\circ$  axis from the disk midplane is given by the disk pressure scale height. See Section 2 for more details.

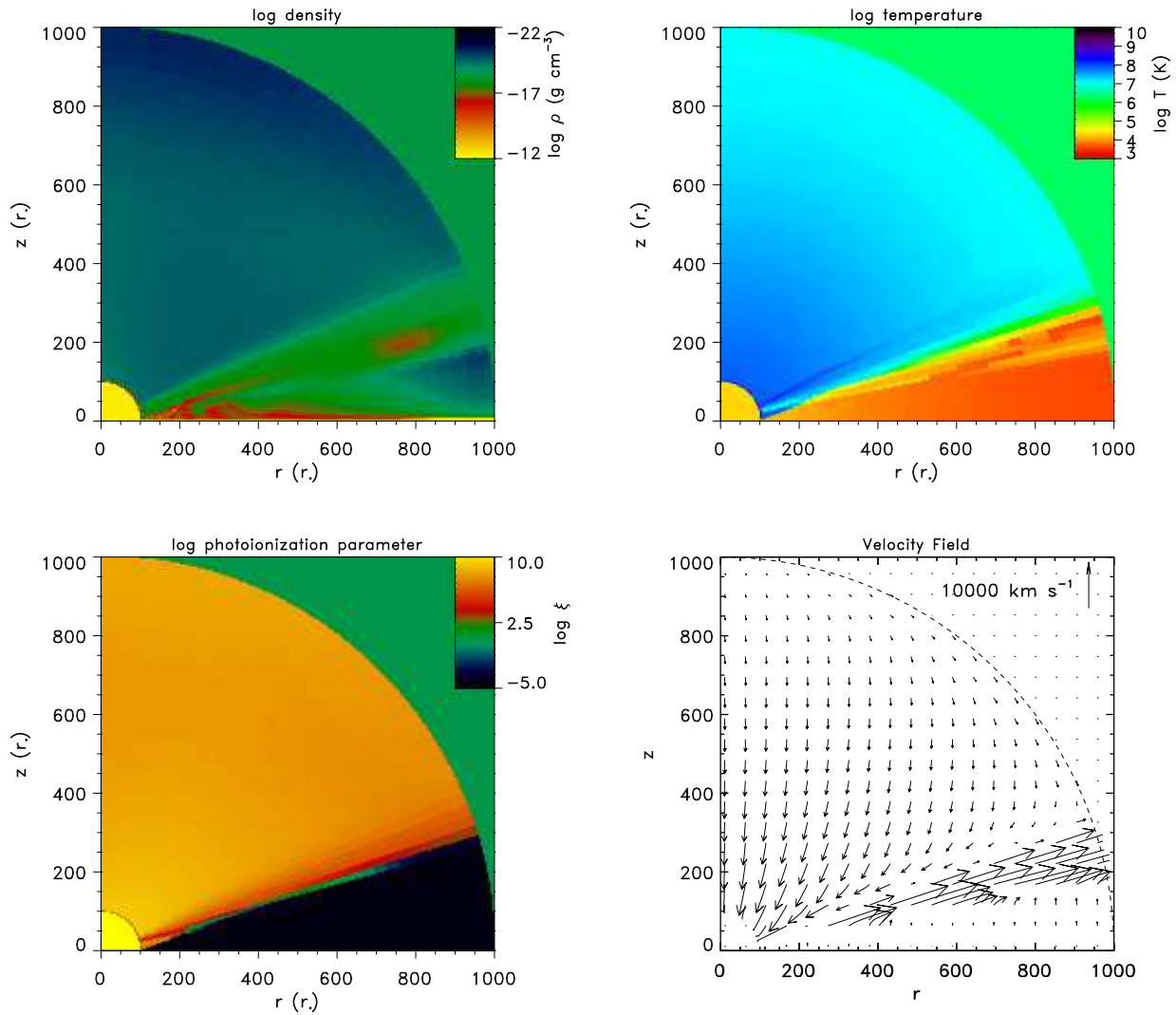


Fig. 2.— The top left panel is a color density map of the AGN disk wind model, described in the text. The top right panel is a color gas temperature map of the model while the bottom left panel is a color photoionization parameter map. Finally, the bottom right panel is a map of the velocity field (the poloidal component only). In all panels the rotation axis of the disk is along the left hand vertical frame, while the midplane of the disk is along the lower horizontal frame.

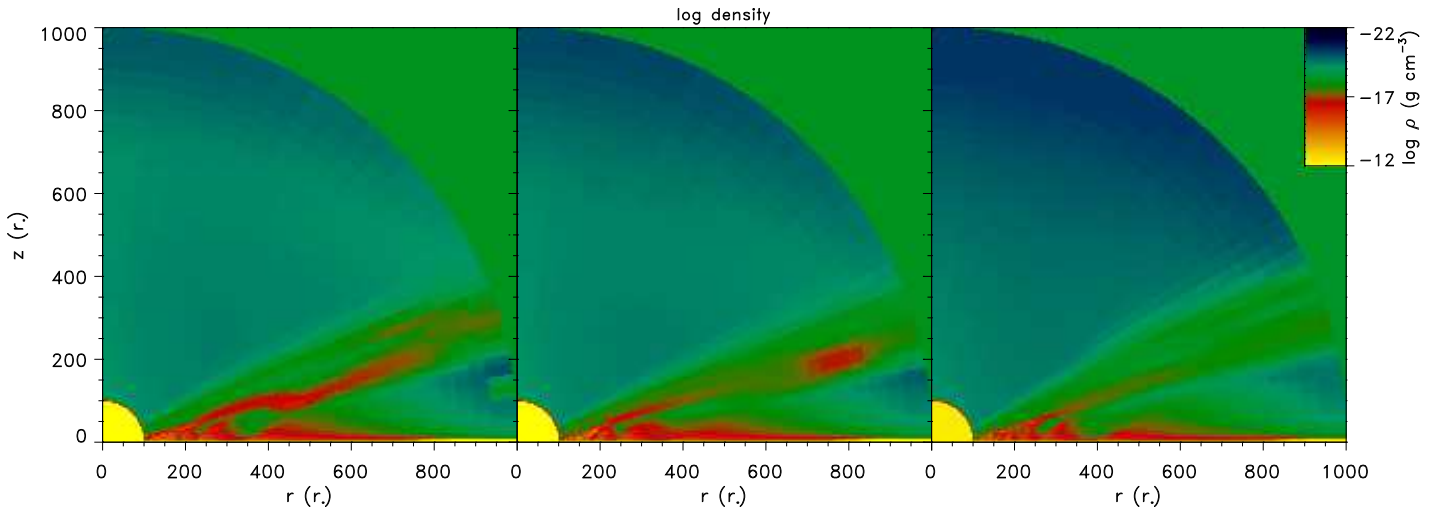


Fig. 3.— A sequence of density maps for the model from Figure 2 after 13.3, 14.6, and 16.47 years (left, middle, and right panel). Note both the time-dependent fine structure near the base of the wind and the time-dependent large scale structure associated with the fast stream at the polar angle  $\sim 75^\circ$

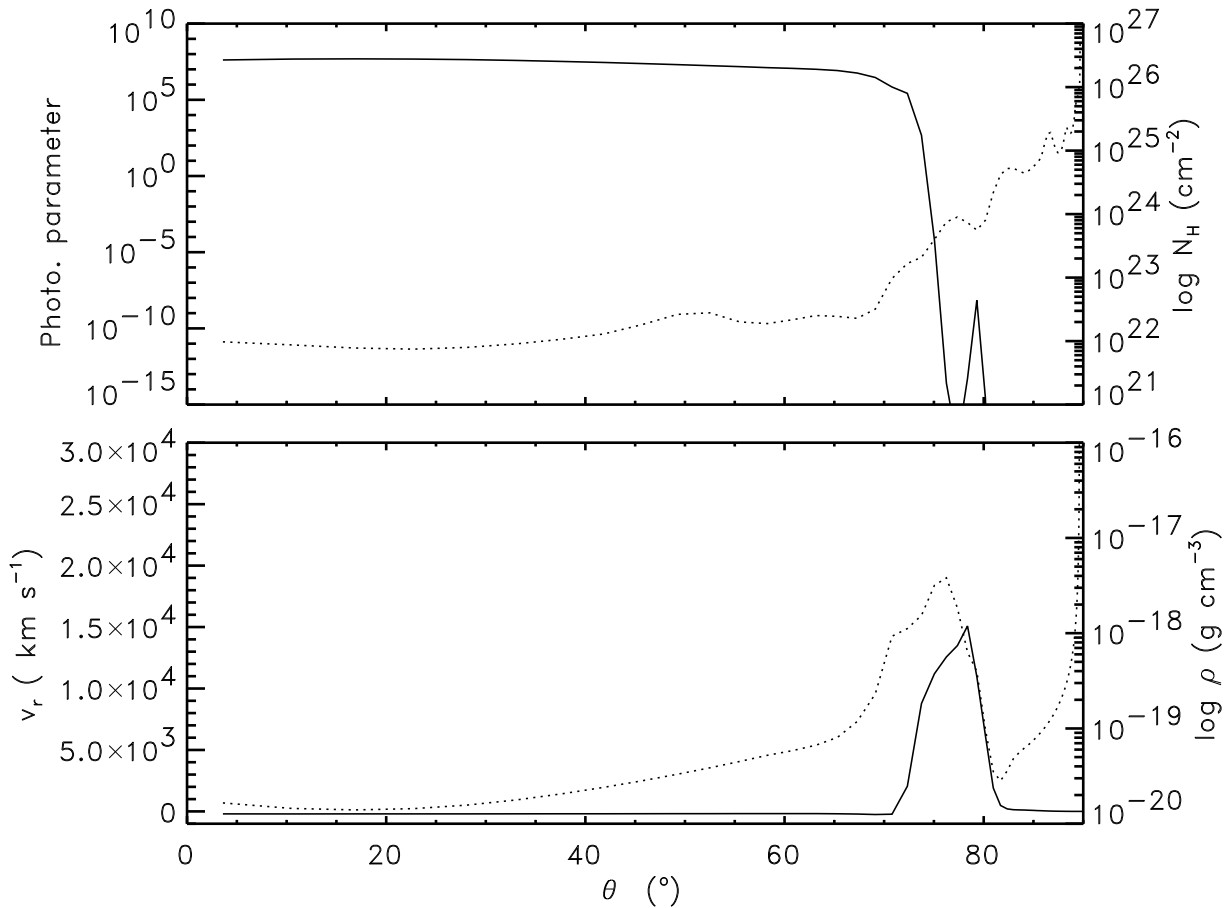


Fig. 4.— Quantities at the outer boundary in our model (the top left panel of Figure 2 and the middle panel of Figure 3). The ordinate on the left hand side of each panel refers to the solid line, while the ordinate on the right hand side refers to the dotted line. The column density,  $N_H$  is calculated along the radial direction. The radial velocity peaks at  $\theta \approx 74^\circ$  while the density at  $\theta \approx 71^\circ$ . The column density is less than  $10^{24} \text{ cm}^{-2}$  for  $\theta \lesssim 80^\circ$ .